J. Fluid Mech. (2024), *vol*. 996, A6, doi:10.1017/jfm.2024.720

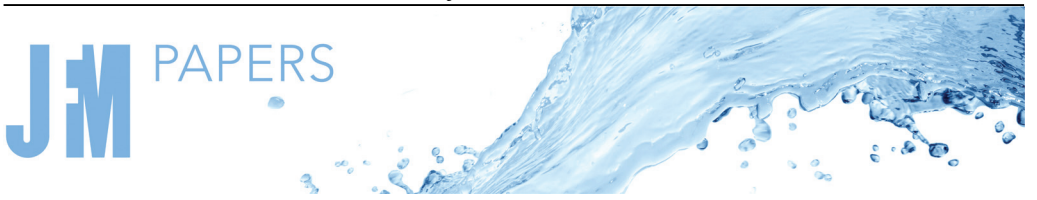

Mechanism of enhanced impulse and entrainment of a pulsed jet through a flexible nozzle

Daehyun Choi[1] **and Hyungmin Park**[1,2,†]

[1]Department of Mechanical Engineering, Seoul National University, Seoul 08826, Korea

[2]Institute of Advanced Machines and Design, Seoul National University, Seoul 08826, Korea

(Received 30 December 2023; revised 29 April 2024; accepted 12 June 2024)

The present experimental study shows that a nozzle with optimal flexibility can enhance the impulse and entrainment of a pulsed jet. Near the nozzle exit, vortex rings emanating from the flexible nozzle move faster because of the timely release of the elastic energy (stored during the expansion) to the jet, which is maximized at the structural stiffness that needs to be optimally tuned to the jet acceleration. The total circulation, hydrodynamic impulse and entrained fluid volume are enhanced substantially. Interestingly, we find that the same condition for optimal flexibility to maximize the hydrodynamic impulse and circulation of the primary vortex ring of the continuous jet (Choi & Park, *J. Fluid Mech.*, vol. 949, 2022, A39) holds universally for the pulsed jet, indicating that abrupt jet termination is irrelevant to the impulse augmentation mechanism. Compared to the rigid counterpart, increments of the impulse (∼400 %) and entrainment (∼220 %) of a pulsed jet in the present study are considerably larger than those (200 % and 50 %, respectively) in a continuous jet from previous studies, which is attributed to the significant suppression of negative pressure at the nozzle exit by the collapsing motion of the flexible nozzle in the phase with the jet-driven upstream propagation of the surface wave on the nozzle. This universal mechanism provides a guideline for a novel jet propulsor using a flexible nozzle, for example, for small-scale underwater robots.

Key words: flow-structure interactions, jets

† Email address for correspondence: hminpark@snu.ac.kr

1. Introduction

A pulsed jet is characterized by the ejection of the finite volume of a fluid with a high momentum into the surroundings, which is widely utilized in nature and industry. Underwater animals such as cephalopods and salps use pulsed jets through their funnels for locomotion (O'Dor, Pörtner & Shadwick 1990; Staaf, Gilly & Denny 2014; Bujard, Giorgio-Serchi & Weymouth 2021), and archerfish use them to catch terrestrial insects (Gerullis & Schuster 2014). The bombard beetle rapidly ejects a hot fluid jet generated by a chemical reaction towards predators, as a type of defence mechanism (Arndt *et al.* 2015). In industry, pulsed jets are used to clean the filtration or inject fuel into the reaction chamber of a gasoline engine (Shim, Joe & Park 2017). Recently, the pulsed-jet reactor for biofuel was actively studied because of its high efficiency, simple design and robust operation (Schott *et al.* 2022).

The rich physics related to the pulsed jet has led to active investigations. The hydrodynamics of a pulsed jet can be characterized by the impulse and jet entrainment, which depend on the nozzle geometry, working fluid (e.g. multiphase flow), jet condition (e.g. acceleration time), and so on. The increase rate of the jet impulse is the sum of the jet momentum ($\sim\rho_f v^2 A$, where ρ_f, v and A denote the fluid density, jet velocity and area at the nozzle exit, respectively) and the jet-exit pressure ($\sim(p-p_\infty)A=\Delta p\,A$, where p and p_∞ correspond to the fluid pressures at the exit and remote location, respectively) (Krueger & Gharib 2003; Krieg & Mohseni 2013). The jet momentum depends only on the piston motion when the nozzle and piston are rigid; however, the exit pressure (p) can vary according to the jet-vortex dynamics (Gao *et al.* 2020; Limbourg & Nedić 2021). For example, the formation of a primary vortex ring and the subsequent reinforcement of the jet (contributed by Δp) from a rigid cylindrical nozzle can be maximized when the formation number F ($=L_p/D_p$, where L_p and D_p represent the stroke and diameter of the piston, respectively) is ∼3–4 (Gharib, Rambod & Shariff 1998; Krueger & Gharib 2003). Krieg & Mohseni (2013) showed that radial flow near the nozzle exit increases the contribution of Δp to the jet impulse, thereby resulting in a 70–75 % increment. The enhanced impulse is associated with the faster jet acceleration because of the larger added-mass effect attributed to the entrainment near the jet exit (Gao *et al.* 2020). As an attempt to control the dynamics of the jet vortices, Dabiri & Gharib (2005) showed that the closing and opening of the nozzle exit during jet ejection can increase vortex circulation by up to 35 % (and the jet entrainment up to 5 %).

Recently, given the increasing interest for soft materials, a universal optimal flexibility condition for maximizing the thrust of a continuous jet, which enabled achieving more than a 100 % increase in the hydrodynamic impulse compared to the rigid counterpart, was reported (Choi & Park 2022). Although previous investigations tended to simply conclude that jet flow is accelerated with a flexible nozzle (Dabiri & Gharib 2005; Das, Govardhan & Arakeri 2018), the quantified criterion is meaningful to design nozzle flexibility based on the flow conditions. The augment of impulse by the flexible nozzle is directly associated with the nozzle–jet interaction, i.e. fluid–structure interaction. The nozzle expands because of the positive pressure generated from the moving piston when the flow inside the nozzle starts to accelerate, and this appears as the expansion wave propagating along the nozzle. The wave bounces back when it reaches the nozzle exit, from which nozzle contraction begins. The time scale for this nozzle deformation (time required for the expansion and contraction waves to travel) is determined by the wave speed (i.e. flexibility) and nozzle length. Choi & Park (2022) suggested that the jet impulse is maximized when this time scale is tuned with the jet acceleration time, for maximizing the jet velocity.

This analysis was validated for the continuous jet, i.e. the flow is accelerated continuously inside the nozzle. In contrast, for the pulsed-jet condition, the flow inside the nozzle should decelerate abruptly, producing a negative pressure inside the nozzle and inducing a corresponding contraction wave moving on the nozzle surface. Assisted by this nozzle deformation, the pulsed jet can probably induce additional fluid motion, thereby affecting jet characteristics such as impulse and entrainment. Additionally, the characteristics of the jet flows (e.g. dynamics of jet vortices) related to the thrust or entrainment of the jet are considerably different based on the formation number (Gharib *et al.* 1998). Therefore, in this study, we investigate the fluid–structure interaction between the flexible nozzle and pulsed jet in terms of the resulting hydrodynamic impulse and jet entrainment. The validity of the optimal flexibility condition derived for the maximum thrust of the continuous jet (Choi & Park 2022) is examined, and the underlying physics is discussed.

2. Experimental set-up and procedure

We used the same flow facility to create a pulsed jet and employ the measurement technique used in the previous study (details can be found in Choi & Park 2022). The pulsed jet is generated by the piston–motor system through the nozzle and fed into a water tank ($300 \times 300 \times 700$ mm^3; figure 1*a*). The 50 mm diameter piston pressurizes the water inside the cylindrical nozzle, actuated by a linear guide and a 40 W motor (ELDM6020, LeadShine). The motor driver (ELD5-400, LeadShine) controls the piston motion to precisely accomplish the desired history of jet-exit velocity (v_e) (see the supplementary material and movies, available at https://doi.org/10.1017/jfm.2024.720, for the repeatability test of the present jet generator). The centre of the undeformed nozzle exit is designated as the origin. Keeping the piston stroke the same, i.e. the volume of displaced water (V_p), three pulsed-jet velocity profiles are generated by controlling both the speed and the response time of the motor (figure 1*d*). In the figure, the effective acceleration time of the pulsed jet is defined as $\Pi_0 = v_{m,r}T_{acc}/L$ (Choi & Park 2022). For $\Pi_0 < 1.0$ ($T_{acc} < L/v_{m,r}$), which is the case for the present conditions, the transient behaviour of the flexible nozzle is more dominant. The jet acceleration time (T_{acc}), defined as the time when v_e reaches the maximum value ($v_{m,r}$) for the rigid nozzle, varies as 0.05–0.16 s, and the Reynolds number ($Re = v_{m,r}D/\nu$, where D and ν denote the inner nozzle diameter and the kinematic viscosity of water, respectively) is in the range 1500–4500.

The flexible nozzle is a 30 mm long hollow circular cylinder made of transparent elastomer (SortaClear 40A, SmoothOn) with inner diameter 15 mm. The detailed manufacturing process is explained in Choi & Park (2022). The structural stiffness ($Eh = 7.0, 14.4, 43.2$ N m^{-1}) of the flexible nozzle is defined with a Young's modulus (E) measured by calculating the slope of the stress–strain curve obtained from the tensile test and the averaged nozzle thickness (h) along the nozzle length (see § 2.2 in Choi & Park 2022). For the present flexible nozzles, the wall is sophisticatedly controlled to be sufficiently thin (100–500 μm) to expand by the accelerating jets. The thin-walled elastomer is connected to the relatively thicker supporting elastomer (made of the same material as the thin one) to avoid a strain-rate concentration that causes ripping (figure 1*b*). As demonstrated, the doughnut-shaped stainless steel support mounted on the flange robustly holds the flexible nozzle during the rapid acceleration and deceleration (figure 2*a*), which enables the accurate measurement of the fluid–structure interaction between the flexible nozzle and pulsed jet.

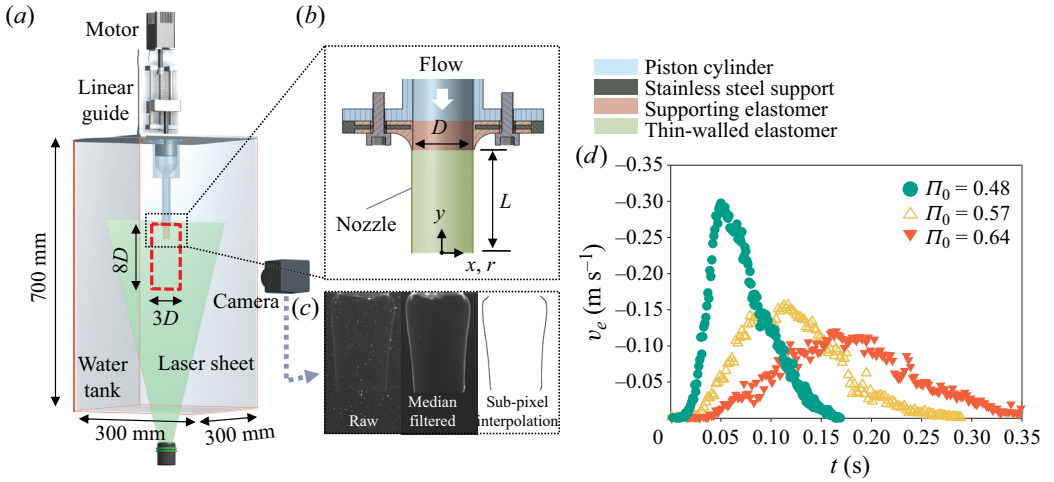

Figure 1. (*a*) Schematic for the jet flow facility. (*b*) Installation set-up of the flexible nozzle. (*c*) Image processing procedure for obtaining the sub-pixel location of the nozzle. (*d*) Three histories of the centreline jet velocity at the nozzle exit, depending on an effective acceleration time ($\Pi_0 = v_{m,r}T_{acc}/L$).

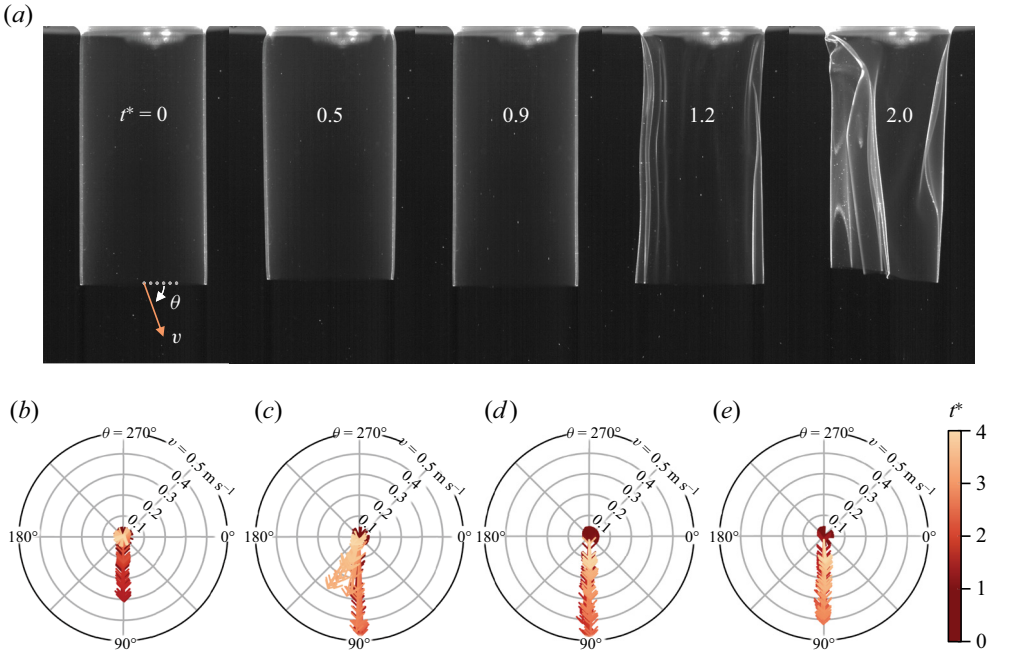

Figure 2. (*a*) Variation in the shape deformation of the most flexible nozzle ($Eh = 7.0$ N m^{-1}) in time ($t^* = t/T_{acc}$), corresponding to $\Pi_0 = 0.57$. (*b–e*) Temporal variations in the jet velocity vector at the centre of the nozzle exit ($x = y = 0$) depending on nozzle stiffness (Eh): (*b*) $Eh = \infty$ (rigid); (*c*) $Eh = 43.2$ N m^{-1}; (*d*) $Eh = 14.4$ N m^{-1}; (*e*) $Eh = 7.0$ N m^{-1}. The colour denotes the time.

Glass particles (50 μm, HSG-10, Dantec Dynamics) are seeded into the flow as a tracer, and illuminated by the green-coloured laser sheet (RayPower 5000, Dantec Dynamics) to perform particle image velocimetry at the centre plane ($z = 0$). The

high-speed camera (NX5, IDT) captures particle images at rate 500–1000 Hz with sensor size 375 × 1000 pixels ($3D \times 8D$) (figure 1*a*). As illustrated in figure 1(*c*), the raw image is processed to highlight the nozzle wall, and its sub-pixel location is calculated using Gaussian interpolation. The particle-only image is obtained for the velocity fields by subtracting the pixel intensity corresponding to the nozzle wall from the raw image. We used the two-stage (64 × 64 to 32 × 32 interrogation windows) cross-correlation technique to evaluate the velocity vectors, which was proven to effectively reduce particle loss or influx within the interrogation window, making the algorithm robust and precise for application to high-shear flows (Choi & Park 2018, 2021, 2022). The number of the resultant velocity vectors is approximately 1800 (spatial resolution 56.3 μm pixel^{-1}), and the uncertainty is estimated within 5 % based on the error propagation theory (Maeng & Park 2021).

Following Choi & Park (2022), we define the effective nozzle stiffness ($\Pi_1 = Eh/(\rho_f v_{m,r}^2 R)$) by normalizing structural stiffness (Eh) with the jet momentum, where $v_{m,r}$ and R denote the maximum jet-exit velocity and inner radius of the rigid nozzle, respectively. This parameter represents the ratio of the tensile stress ($\sim Eh\,R$) of the expanded nozzle to the fluid pressure ($\sim \rho_f v_{m,r}^2 R^2$) acting on the nozzle cross-sectional plane. The dimensionless wave speed ($\hat{c} = cT_{acc}/L$) is defined based on the physical (dimensional) wave speed $c = \sqrt{Eh/(\rho_f D)}$, which is normalized by the nozzle length (L) and acceleration time (T_{acc}). That is, it is the ratio of wave speed to the characteristic velocity (L/T_{acc}), which results in the dimensionless form $\hat{c} = \sqrt{Eh\,T_{acc}^2/(\rho_f D L^2)} = \sqrt{\Pi_0^2 \Pi_1/2}$. These three parameters are derived analytically from the mass and momentum conservation equations for the fluid inside the deforming flexible nozzle, and the optimal condition for the maximum thrust is found to be $\hat{c} \simeq 3.0$ (Choi & Park 2022). In this study, the effective acceleration time (Π_0) and effective nozzle stiffness (Π_1) are in the ranges 0.48–0.64 and 11–400, respectively. Accordingly, the dimensionless wave speed ($\hat{c}$) encompasses the optimal value, in the range 1.1–16.0, using which the nozzle and jet behaviour near and off the optimal conditions can be compared. In addition, we varied the formation number in the range $F = 2.2$–8.9 to observe the effect of piston stroke on the fluid–structure interaction mechanism found in this study.

3. Results and discussion

Figure 2(*a*) illustrates the representative deformation of the most flexible nozzle ($Eh = 7.0$ N m^{-1}) corresponding to the intermediate jet acceleration of $\Pi_0 = 0.57$. The temporal variations of jet-exit velocity at the centre ($x = y = 0$) are plotted with the polar angle (θ) (defined in figure 2*a*) for various Eh (figures 2*b–e*). In figure 2(*a*), the side edges of the deformed nozzle are illuminated by the laser sheet on the x–y plane. During the jet acceleration ($t^* < 1.0$), the cylindrical nozzle expands radially (see $t^* = 0.5$) and contracts ($t^* = 0.9$) to its original shape. After the jet starts to decelerate ($t^* > 1.0$), the nozzle contracts further by the negative pressure inside the nozzle, leading to a buckled state ($t^* = 1.2$), and subsequently, irregular foldings occur ($t^* = 2.0$). During the nozzle deformation before complete folding, the jet-exit velocity always aligns with the y-axis (i.e. $\theta = -90°$) for all nozzle stiffnesses $Eh = \infty$, 43.2, 14.4, 7.0 N m^{-1} (and all jet conditions $\Pi_0 = 0.48$–0.64), which indicates that the jet flow keeps the axisymmetry (the cases for $\Pi_0 = 0.48$ are shown in figures 2*b–e*). A slight deviation occurs at the least flexible nozzle ($Eh = 43.2$ N m^{-1}) because of the weak jet momentum at $t^* > 3.0$ (figure 2*c*), which is far after the end of the acceleration. However, for all cases in the present study, the

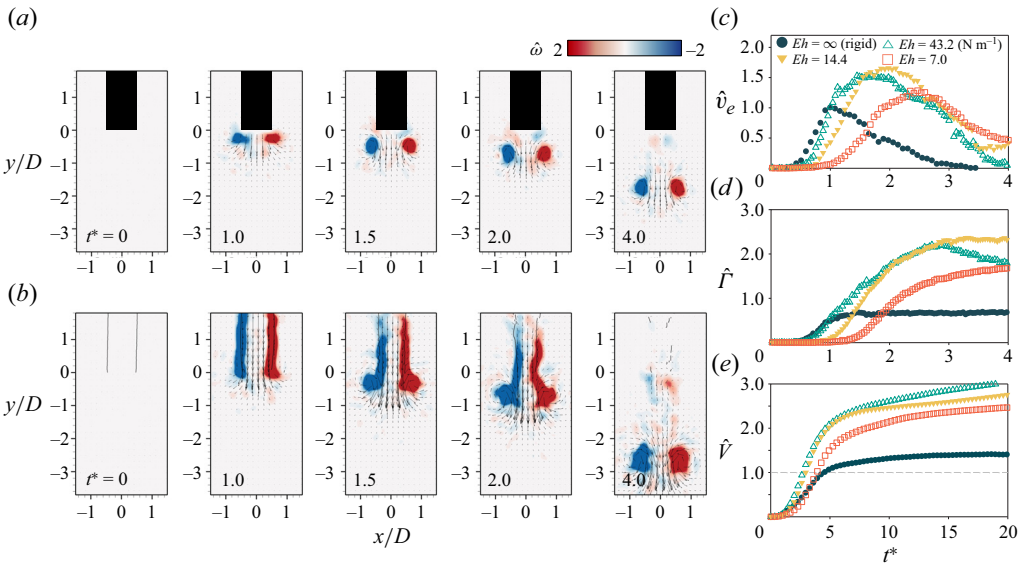

Figure 3. (*a*,*b*) Evolution of the vorticity ($\hat{\omega} = \omega D/v_{m,r}$) contour and velocity vectors in a pulsed jet with the fastest acceleration ($\Pi_0 = 0.48$) for (*a*) rigid and (*b*) flexible ($Eh = 14.4$ N m^{-1}) nozzles. (*c–e*) Temporal variation of: (*c*) the centreline velocity ($\hat{v}_e = v_e/v_{m,r}$) at the nozzle exit ($y = 0$) normalized with the maximum value for the rigid nozzle ($v_{m,r}$); (*d*) normalized total circulation ($\hat{\Gamma} = \Gamma/(v_{m,r}D)$); (*e*) normalized total jet volume ($\hat{V} = V/V_p$), where V_p represents the displaced volume by piston. The dimensionless time is defined as $t^* = t/T_{acc}$.

flow and nozzle deformation remain axisymmetric for $t^* < 2.0$ and $t^* < 1.0$, respectively. Thus in the following analysis, it is assumed that the jet flow and nozzle deformation are approximately axisymmetric.

Typical evolution of the pulsed jet from the rigid nozzle for the fastest acceleration of $\Pi_0 = 0.48$ is shown in figure 3(*a*). After the piston starts to accelerate at t^* ($= t/T_{acc}$) $= 0$, the shear layer is fed into the ambient fluid near the exit, and forms the vortex ring at $y/D = -0.2$. As the jet decelerates at $t^* = 1.0$, the vortex ring detaches from the nozzle exit (see $t^* = 1.5$). The negative pressure is developed inside the nozzle by the sudden flow stall inside the nozzle and the flow induced downstream by detached vortex ring, thereby resulting in the suction of ambient flow into the nozzle (Gao *et al.* 2020). Consequently, the secondary counter-rotating vortex ring appears at the nozzle exit ($t^* = 2.0$). When $t^* > 2.0$, the secondary vortex is entrained into the nozzle, and the primary vortex ring becomes completely isolated and moves downstream (see supplementary material and movie 1 for the detailed movements of the jet vortices). There is no trailing jet behind the primary vortex because the present formation number ($F = 2.7$) is sufficiently smaller than the critical value ($F = 4$), above which the vortex ring detaches spontaneously by the excessive supply and accumulation of vorticity (Gharib *et al.* 1998; Krueger & Gharib 2003).

The jet vortices from the flexible nozzle are significantly intensified, and their dynamics are considerably altered (figure 3*b*). During the acceleration ($t^* < 1.0$), the nozzle expands radially because of positive pressure inside, building tensile stress along the nozzle wall. Consequently, a portion of the work done by the piston is stored as elastic energy and used to increase the jet kinetic energy. The jet-exit velocity ($\hat{v}_e = v_e/v_{m,r}$) of the flexible nozzle with $Eh = 14.4$ N m^{-1} is temporally slower than the rigid one at $t^* < 1.0$ because of the

redistribution of energy (figure 3*c*). The stored elastic energy is released to supplement the jet kinetic energy, and $\hat{v}_e$ increases by ∼170 % (for $Eh = 14.4$ N m^{-1}) compared to the maximum value for the rigid nozzle at $t^* = 2.0$, at which the jet-exit velocity of the rigid nozzle has been reduced substantially. Contrary to the rigid nozzle, the counter-rotating secondary vortex ring is not induced at the exit of the flexible nozzle (see $t^* = 2.0$ in figure 3*b*), which indicates that the negative pressure is negligible or suppressed by nozzle shrinkage. This collapse behaviour (figure 2*a*) is responsible for the difference in jet vortex dynamics, i.e. additional fluid induced towards the jet direction is entrained into the primary vortex ring ($t^* = 4.0$ in figure 3*b*) and further increases the circulation of the primary vortex ring at $t^* > 1.0$ (figure 3*d*). Here, the nozzle collapses inwardly after contracting beyond its original shape ($t^* > 1.0$ in figure 2*a*), since the buckled structure attributed to the bending has a smaller energy state than maintaining the axisymmetric shape (Kraus 1967). Considering the considerably thin wall of the present nozzle ($h \sim O(10^2)$ μm), the bending force ($\sim h^3$) on the wall is far smaller than the tensile force ($\sim h^2$), indicating that the collapsing motion would exert negligible fluid pressure to the surrounding fluid compared to the expansion–contraction behaviour. Thus the flexible nozzle acts as if it vanished during the deceleration stage, effectively suppressing the negative pressure that mitigates the jet velocity and vortex circulation (Krueger & Gharib 2003; Gao *et al.* 2020).

In figures 3(*c–e*), we compared the jet characteristics in terms of the exit velocity, total circulation and total jet volume, according to Eh. The case $Eh = \infty$ denotes the rigid nozzle. In figure 3(*d*), the total circulation is defined as $\Gamma = \int_{S^+} \omega \, \mathrm{d}A$, where S^+ is the region $0 < x/D < 1.5$ and $-8 < y/D < 0$, in which half of the counter-rotating vortex ring moves downstream. The jet volume (figure 3*e*) passing through $y/D = -1.0$ is calculated as $V = \int_0^t \int_{-1.5D}^{1.5D} v(2\pi x) \, \mathrm{d}x \, \mathrm{d}t$, where v represents the vertical velocity, and is further normalized by the volume displaced by piston movement (V_p), as $\hat{V} = V/V_p$. Thus $\hat{V}$ shows the entrainment rate compared to the volume supplied by the piston motion. In figure 3(*d*), the flexible nozzle substantially increases the maximum centreline velocity (v_e), total circulation (Γ) and total jet volume (V), compared to the rigid nozzle. They are not monotonically enhanced with the flexibility. For the cases shown, the maximum increase in the exit velocity and circulation is achieved at $Eh = 14.4$ N m^{-1} (see inverted triangle symbols in figures 3*c*,*d*).

Thus the dependency on flexibility changes according to the input jet condition (Π_0). In figure 4, we compared the hydrodynamic impulse ($\hat{I}_h = I_h/(v_{m,r}D^3)$), maximum centreline velocity at nozzle exit ($\hat{v}_m = v_m/v_{m,r}$), total circulation ($\hat{\Gamma} = \Gamma/(v_{m,r}D)$) and total fluid volume ($\hat{V} = V/V_p$) passing through $y/D = -1.0$, depending on Eh and Π_0. The hydrodynamic impulse (I_h) was calculated as $I_h = 0.5\rho_f \int_C \boldsymbol{x} \times \boldsymbol{\omega} \, \mathrm{d}V$ (Saffman 1955). Here, $\boldsymbol{x} = (r, \theta, y)$ denotes the position vector originating from the centre of the nozzle exit (as shown in figure 1*b*), and $\boldsymbol{\omega} = (\omega_r, \omega_\theta, \omega_y)$ represents the vorticity vector. Given the axisymmetric nature of the flow ($\omega_r = \omega_y = 0$) and the differential volume $\mathrm{d}V = 2\pi r \times \mathrm{d}A$, the hydrodynamic impulse simplifies to $I_h = 0.5\pi\rho_f \int_C r^2 \, |\omega_\theta(r, y)| \, \mathrm{d}A$. The control surface C is in the ranges $-2 \leq x/D \leq 2$ and $-5.5 \leq y/D \leq 0$ in the measurement plane, excluding the area inside the nozzle located at $y/D > 0$, and ω_θ represents the vorticity component perpendicular to the measurement plane. Also, $\hat{I}_h$ and $\hat{\Gamma}$ are measured at $t^* = 4.0$, and $\hat{V}$ at $t^* = 20.0$, after which they converge. For $\Pi_0 = 0.48$, when the pulsed jet accelerates the fastest (figure 3), the nozzle with $Eh = 14.4$N m^{-1} outperforms the nozzles that are more ($Eh = 7.0$ N m^{-1}) and less

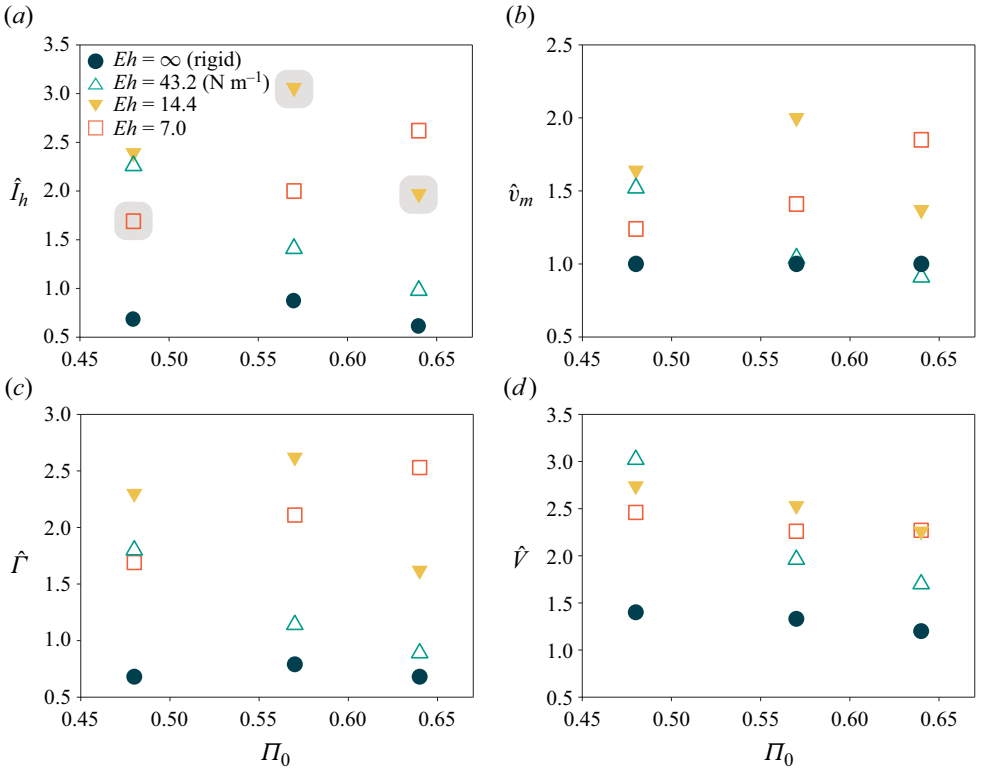

Figure 4. Variation of (*a*) hydrodynamic impulse ($\hat{I}_h = I_h/(v_{m,r}D^3)$) at $t^* = 4.0$, (*b*) maximum centreline velocity ($\hat{v}_m = v_m/v_{m,r}$), (*c*) total circulation ($\hat{\Gamma} = \Gamma/(v_{m,r}D)$) at $t^* = 4.0$, and (*d*) total jet volume ($\hat{V} = V/V_p$) at $t^* = 20.0$, depending on Π_0 and Eh. The shaded symbols in (*a*) correspond to cases used to further examine the nozzle deformation in figure 5.

($Eh = 43.2$ N m^{-1}) flexible. The maximum centreline velocity shows a strong correlation with the impulse and circulation (figures 4*a–c*) because the growth rates of both hydrodynamic impulse $\mathrm{d}I_h/\mathrm{d}t \sim \rho_f v_e^2 A$ (Gao *et al.* 2020) and circulation $\mathrm{d}\Gamma/\mathrm{d}t \sim v_e^2/2$ (Krieg & Mohseni 2013) scale with the jet-exit velocity (v_e^2). The jet volume has less variation ($\Delta\hat{V} < 1.0$) among different flexibilities (except for the rigid nozzle) under the same jet condition (figure 4*d*). However, it increases with decreasing Π_0 because of a larger amount of entrainment into the vortex ring by the faster acceleration (Ruiz, Whittlesey & Dabiri 2011). As Π_0 increases to 0.57 and 0.64, the maximum velocity ($\hat{v}_m$) of the least flexible nozzle ($Eh = 43.2$ N m^{-1}) becomes comparable to the rigid nozzle (figure 4*b*) because the weakened acceleration is not sufficient to expand the stiff nozzle. However, the impulse and circulation are still slightly higher than the rigid nozzle (figures 4*a*,*c*), which is attributed to the additional fluid supplied during the nozzle collapse at $t^* > 1.0$. For this weakly accelerated condition ($\Pi_0 = 0.57$–0.64), softer nozzles with $Eh = 7.0$ and 14.4 N m^{-1} are still sufficiently flexible to amplify the kinetic energy of the jet. For the weakest acceleration ($\Pi_0 = 0.64$), the optimal flexibility transitions to $Eh = 7.0$ N m^{-1}, supporting our claim on the optimal flexibility coupled with the flow condition.

To understand the underlying fluid–structure interaction, the radial displacement (w_n) of the nozzle is measured along the nozzle length (y) and time (t) with resolution $0.004D$ ($= 60$ μm) (figure 5*a*). Figures 5(*b*,*d*,*f*) show the overlay of nozzle edge profiles at

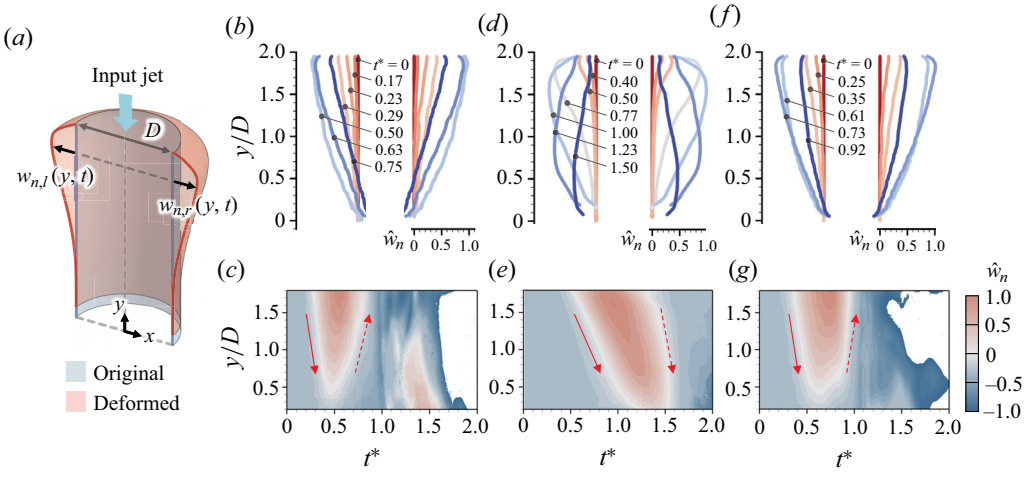

Figure 5. (*a*) Schematic of nozzle displacement ($w_{n,r}$ for $x > 0$, and $w_{n,l}$ for $x < 0$) perpendicular to the original surface in the cross-sectional (x–y) plane. (*b*,*d*,*f*) Overlay of nozzle edge profiles ($\hat{w}_n$) at various t^*, and (*c*,*e*,*g*) spatio-temporal variation of the nozzle deformation ($\hat{w}_n$) depending on Eh and Π_0. Here, (*b*,*c*) (Eh, Π_0) = (14.4 N m^{-1}, 0.64), (*d*,*e*) (7.0, 0.48), (*f*,*g*) (14.4, 0.57). The normalized nozzle deformation is defined as $\hat{w}_n = 0.5(w_{n,r} + w_{n,l})/w_{n,m}$, in which the maximum value ($w_{n,m}$) is 0.016D, 0.153D and 0.038D for (*b*,*c*), (*d*,*e*), and (*f*,*g*), respectively. In (*b*,*d*,*f*), the variation of $\hat{w}_n$ along the y-direction is shown at both sides for visualization.

various instants ($t^* < 2.0$), and figures 5(*c*,*e*,*g*) present the corresponding spatio-temporal contours of nozzle deformation ($\hat{w}_n$) depending on Eh and Π_0. The nozzle tends to deform axisymmetrically until buckling ($t^* < 1.0$), therefore the displacements measured at two sides (i.e. $w_{n,r}$ and $w_{n,l}$ in figure 5*a*) were averaged and normalized by the maximum value ($w_{n,m}$), as $\hat{w}_n = 0.5(w_{n,r} + w_{n,l})/w_{n,m}$. The white area in figures 5(*c*,*e*,*g*) represent the data removed because of the noise caused by light refraction from the wrinkled surface. For clear comparison, figures 5(*b*,*c*) and 5(*d*,*e*) show cases with lower jet impulse, while the optimal case for maximum impulse is shown in figures 5(*f*,*g*) (all values are highlighted with a shadow in figure 4(*a*), and the nozzle deformations in each case are shown in the supplementary material and movie 2). For (Eh, Π_0) = (14.4 N m^{-1}, 0.64) (figures 5*b*,*c*), the nozzle expansion wave (red region) propagates from the support ($y/D = 2.0$) to the tip ($y/D = 0$) with a constant speed (visualized in figure 5(*b*) at $t^* < 0.6$ and indicated by a solid arrow in figure 5*c*), and it bounces back at $t^* = 0.8$ (dashed arrow in figure 5*c*), along which the contraction occurs (blue region in figure 5*c*). The wave speed (c) on the nozzle surface increases with Eh but decreases with the fluid inertia ($\rho_f D$), expressed as $c = (Eh/\rho_f D)^{0.5}$ (Avrahami & Gharib 2008; Choi & Park 2022). Choi & Park (2022) suggested that the thrust of the continuous jet is maximized when the travel time of the wave along the nozzle matches the jet acceleration time, resulting in the constant dimensionless wave speed ($\hat{c} = cT_{acc}/L \simeq 3.0$ from their measurements). In figures 5(*b*,*c*), $\hat{c} = 5.3$ indicates that the surface wave moves faster than the jet, thereby agreeing with the earlier contraction (at $t^* = 0.8$) rather than the end of jet acceleration ($t^* = 1.0$). The elastic potential energy is released before the jet reaches its maximum velocity, therefore the resulting jet impulse is lower than that in the other cases (figure 4*a*). On the other hand, the travel time of the wave is relatively longer than T_{acc}, i.e. $\hat{c} = 1.1$, for (Eh, Π_0) = (7.0N m^{-1}, 0.48) (figures 5*d*,*e*). In this case, the nozzle expands slowly because of its lower stiffness, and the contraction occurs after the jet has decelerated, producing the lower impulse (figure 4*a*). The contraction wave propagates from the nozzle

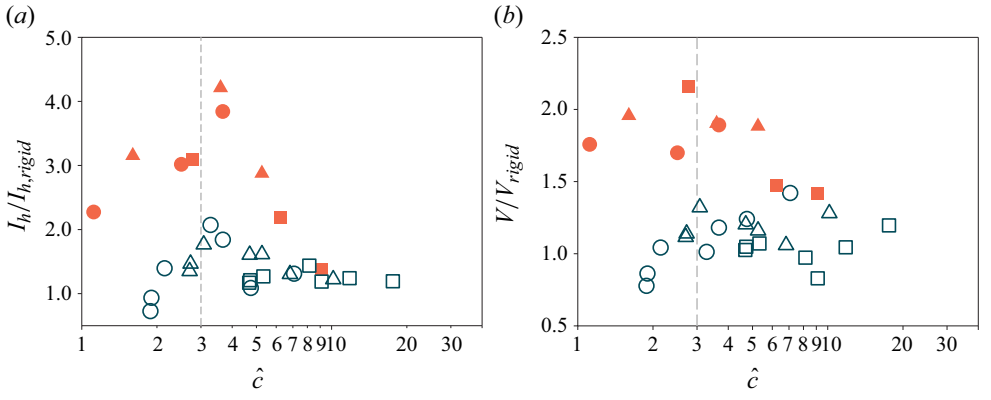

Figure 6. Variation in (*a*) I_h and (*b*) V passing through $y/D = -1.0$ with $\hat{c}$: circle, $Eh = 7.0$ N m^{-1}; triangle, 14.4 N m^{-1}; and square, 43.2 N m^{-1}. Closed and open symbols correspond to the pulsed jet (present study) and continuous jet (Choi & Park 2022), respectively, and I_h and V are normalized with values for the rigid nozzle.

support at $t^* > 1.23$ in figure 5(*d*) (see dashed arrow in figure 5*e*), instead of bouncing back from the nozzle tip. Contrary to these two off-optimal conditions, $(Eh, \Pi_0) = (14.4\ \text{N m}^{-1}, 0.57)$ in figures 5(*f*,*g*) shows that the nozzle contraction ends at $t^* = 1.0$ when the jet has reached the maximum velocity. This condition ($\hat{c} = 2.6$) produces the maximum impulse (figure 4*a*) close to the optimal condition suggested by Choi & Park (2022).

In figure 6(*a*), we compared the hydrodynamic impulse (I_h) normalized by that ($I_{h,rigid}$) of the rigid nozzle depending on $\hat{c}$ for the present pulsed jets, together with the results for continuous jets (Choi & Park 2022). Interestingly, I_h of the pulsed jet is also maximized at $\hat{c} \simeq 3.0$. The impulse decreases sharply at $\hat{c} > 3.0$ because the nozzle becomes too stiff so that the nozzle contracts earlier than the end of acceleration (figure 5*a*). When $\hat{c} > 9.0$, the flexible nozzle behaves almost similar to the rigid one (but the impulse is still increased by the flexible nozzle at this range). When the nozzle becomes too flexible ($\hat{c} < 3.0$), the nozzle contraction is far delayed beyond the instant of the maximum jet velocity (figures 5*f*,*g*). Therefore, the optimal flexibility is irrelevant to the presence of jet deceleration, which is attributed to the fact that the meaningful transfer of elastic energy to the jet kinetic energy occurs at $t^* < 1.0$ before the jet deceleration (figure 5*c*).

Although the presence of the jet deceleration does not affect the optimal condition, the achievable impulse is significantly higher for the pulsed jet, i.e. the advantage of flexibility is more pronounced for the pulsed jet. This can be understood from two aspects that originate from jet deceleration. First, the expanded nozzle is fully contracted to transfer its entire elastic energy to the jet during jet deceleration ($t^* > 1.0$), and second, the nozzle collapse (figure 2*a*) greatly suppresses the negative pressure inside the nozzle. These two effects are limited for the continuous jet because of the subsequent supply of the fluid. Therefore, the maximum 400 % increase of the impulse is achieved, which is remarkable compared to that reported in previous studies (70 % with the orifice nozzle (Krieg & Mohseni 2013) and 5 % with the fast acceleration (Gao *et al.* 2020)). In addition, our preliminary proof-of-concept investigation showed that the flexible nozzle (as a thruster) attached to a small-scale underwater vehicle results in a ∼60 % increase in the translation speed, under the same optimal condition, compared to the body with a rigid nozzle (see supplementary material and movies for the details).

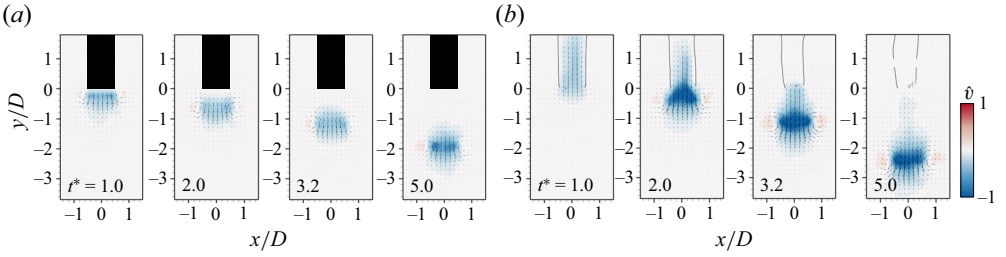

Figure 7. Contours of the vertical flow velocity ($\hat{v} = v/v_{m,r}$) and velocity vectors for (a) rigid and (b) flexible ($Eh = 7.0$ N m^{-1}) nozzles at the same jet condition $\Pi_0 = 0.57$.

The modified vortex dynamics behind the flexible nozzle is associated with the enhanced entrainment of the surrounding fluid. The large jet entrainment is closely relevant to the enhancement of propulsive efficiency by reducing the loss of kinetic energy in the wake (Linden 2011; Ruiz *et al.* 2011). Figure 6(b) shows the jet volume generated by the flexible nozzle relative to the rigid one. Similar to the impulse, the jet volume from the flexible nozzle is increased greatly, which becomes the maximum at $\hat{c} \simeq 3.0$. Only 45 % of the jet volume enhancement was achieved for the cylindrical rigid nozzle with an extremely small formation number $F = 0.5$ (Olcay & Krueger 2008).

Figure 7 shows how jet entrainment is augmented for the flexible nozzle. For the rigid nozzle (figure 7a), the vortex ring stops being fed immediately after the jet ends and moves downstream ($t^* > 1.0$). In contrast, the vortex ring from the flexible nozzle ($Eh = 7.0$ N m^{-1}) is fed for a longer time duration (up to $t^* = 3.2$) during the nozzle collapse, and it grows in higher strength (faster velocity) compared to the rigid nozzle (see $t^* = 5.0$). Similar to the increase in the impulse (figure 6a), the entrainment rate of the pulsed jet is considerably higher than the continuous jet because it is also related to the nozzle collapse, which mitigates the negative pressure. For the present conditions, flexible nozzles with $\hat{c} < 6$ are found to successfully subdue the negative pressure and attain a large entrainment. However, the dependency on the dimensionless wave speed is less salient than that of the hydrodynamic impulse. The entrainment is weakly affected by the jet acceleration, as observed in figure 4(d), therefore other factors such as the nozzle-tip movement (Dabiri & Gharib 2005) and radial velocity at the nozzle exit (Krieg & Mohseni 2013) will be involved, which are less correlated with $\hat{c}$.

We discuss briefly the effect of the formation number (F) on hydrodynamic thrust. Figures 8(a) and 8(b) show instantaneous jet flows at various formation numbers for the rigid and flexible nozzles, respectively, with the nozzle length $L = 0.8D$ (see supplementary material and movie 3 for the jet evolution), and figure 8(c) compares time histories of the jet-exit velocity for $F = 2.2$–8.9 ($\hat{c} = 16$). Here, the flexible nozzle with $L/D = 0.8$ generates the maximum thrust at the optimal condition ($\hat{c} \simeq 3.0$), which is detailed in the supplementary material and movies. For the rigid nozzle (figure 8a), a single vortex ring forms at $F < 4.0$, and a trailing jet with subsequent vortex rings forms above the leading vortex ring at $F > 4.0$, which is consistent with the literature (Gharib *et al.* 1998; Gao *et al.* 2020). For the flexible nozzle (figure 8b), the trailing jet occurs at all F values, indicating the lower critical $F < 3.3$, at which the vortex ring solely occurs. For $F = 3.3$, the trailing jet looks obscure at the instant shown ($t^* = 4.0$) because it is dissipated considerably (the trailing jet for $F = 3.3$ can be seen in the supplementary material and movie 3). The decreased critical formation number was reported in a previous study (Choi & Park 2022) such that the pinch-off location of the jet vortices moved

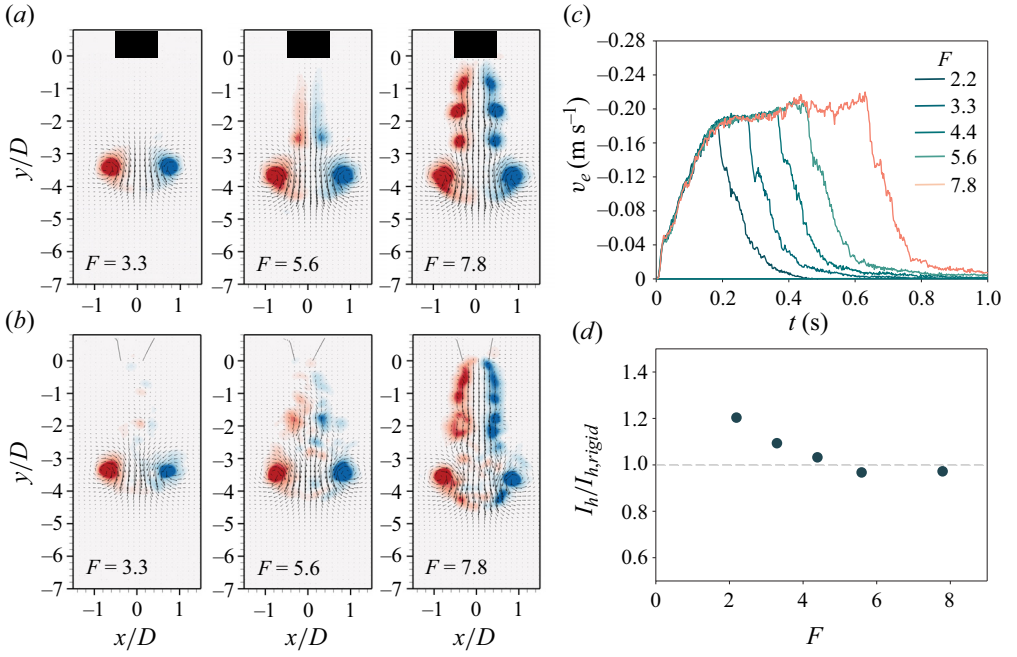

Figure 8. (*a*,*b*) Instantaneous jet flow (velocity vectors and vorticity $\hat{\omega} = \omega D/v_{m,r}$ contour) of (*a*) rigid and (*b*) flexible ($Eh = 14.4\ \mathrm{Nm}^{-1}$) nozzles, depending on the formation number (F), measured at $t^* = 3.6$. (*c*) Time history of the jet-exit velocity (v_e), depending on F. The data were taken at $y/D = -0.2$. (*d*) Hydrodynamic impulse from the flexible nozzle, depending on F. Here, I_h was measured at $t^* = 4$ and normalized by the value of the rigid nozzle ($I_{h,rigid}$).

upwards by 54 % compared to that of the rigid nozzle for $\hat{c} = 7.5$ and $F = 37$ (continuous jet) attributed to the early growth of the jet exit velocity caused by nozzle deformation. Figure 8(*d*) shows the hydrodynamic impulses (I_h) of the flexible nozzles normalized by those of the rigid nozzle ($I_{h,rigid}$) depending on F. Here, I_h was measured at $t^* = 4$. It is observed that $I_h/I_{h,rigid} > 1.0$ for $F < 5.6$ because of the timely nozzle deformation and suppression of negative pressure (i.e. the same fluid–structure interaction mechanism holds); it converges to 1.0 for $F > 5.6$. The value of F at which $I_h/I_{h,rigid}$ saturates to 1.0 is expected to increase as $\hat{c}$ becomes closer to the optimal value ($\simeq 3.0$) (not tested in the present study). In addition, $I_h/I_{h,rigid}$ increases as F decreases because the thrust-augmenting mechanism works at the early stage of jet generation and affects the initial volume of the jet fluid. For the flexible nozzle, the clear relevance between the critical $F = 4$ (for rigid cylindrical nozzle) and thrust enhancement is yet to be found; instead, the maximum thrust is dictated by the optimal condition (figure 6). Although the formation number significantly affects the vortex interaction and its formation, its contribution (up to 10 %) to the total jet impulse (Gao *et al.* 2020) is considerably less than that (400 %) achieved through the optimal flexibility condition of the present study (figure 3*b*).

4. Concluding remarks

In this study, the fluid–structure interaction related to the augmentation of the hydrodynamic impulse and jet entrainment from the flexible nozzle was studied experimentally for the single-stroke pulsed jet. With a rigid cylindrical nozzle as reference,

we considered three flexible nozzles while varying the velocity schedule (i.e. acceleration time) of the pulsed jets. The flexible nozzle enhanced the hydrodynamic impulse and jet entrainment substantially, which were also considerably higher than those achieved for the continuous jet studied in Choi & Park (2022). The measurement of nozzle deformation using the sub-pixel interpolation technique demonstrated that the expansion–contraction wave propagation on the nozzle surface was associated with the determination of optimal flexibility. Interestingly, the optimal condition based on the wave speed holds for both the pulsed and continuous jets, indicating that the presence of the jet deceleration stage was irrelevant to the optimal condition. The large increase in impulse and entrainment can be explained by the beneficial effects of the timely nozzle collapse that amplifies the jet kinetic energy and mitigates the negative pressure attributed to the jet deceleration, inducing the additional entrainment to the primary vortex ring.

The flexible nozzle has a unique capability to amplify the positive pressure at the acceleration stage of the jet and suppress the negative pressure at the deceleration phase. Despite its simple geometry, the flexible nozzle can decouple the acceleration and deceleration jets, which is the inherent limitation of issuing the pulsed jet through a rigid nozzle. Considering the tested Reynolds number range, we believe that the flexible nozzle has the potential to enhance the propulsion performance of small-scale (bio-inspired) underwater vehicles, for which the Reynolds numbers are $O(10–10^4)$ (Moslemi & Krueger 2011; Christianson *et al.* 2020), or help us to understand biological thrusters in nature, such as juvenile squid (Anderson & Grosenbaugh 2005). The current mechanism can be applied to the soft-matter valves to enhance the strength of pulsatile flows in biomedical (Becsek, Pietrasanta & Obrist 2020; Schofield *et al.* 2020) and process engineering where the Reynolds numbers are in a similar range. Finally, the primary mechanisms of enhancing the jet thrust and entrainment are expected to be valid even for higher Reynolds numbers ($>10^4$) compared to those considered in the present study, because the roles of fluid inertia and the tension in the elastic nozzle are dominant factors rather than viscous friction or turbulence, which would be an interesting topic for future work.

Supplementary material. Supplementary material and movies are available at https://doi.org/10.1017/jfm.2024.720.

Funding. This work was supported by research grants (2020R1A2C2014510, 2021R1A4A1032023) through the National Research Foundation of Korea funded by the Korean government (MSIT), and the Institute of Engineering Research at Seoul National University.

Declaration of interests. The authors report no conflict of interest.

Author ORCID.
Daehyun Choi https://orcid.org/0000-0002-5118-4714;
Hyungmin Park https://orcid.org/0000-0003-3525-8573.

References

Anderson, E.J. & Grosenbaugh, M.A. 2005 Jet flow in steadily swimming adult squid. *J. Expl Biol.* **208**, 1125–1146.

Arndt, E.M., Moore, W., Lee, W.K. & Ortiz, C. 2015 Mechanistic origins of bombardier beetle (*Brachinini*) explosion-induced defensive spray pulsation. *Science* **348**, 563–567.

Avrahami, I.D.I.T. & Gharib, M. 2008 Computational studies of resonance wave pumping in compliant tubes. *J. Fluid Mech.* **608**, 139–160.

Becsek, B., Pietrasanta, L. & Obrist, D. 2020 Turbulent systolic flow downstream of a bioprosthetic aortic valve: velocity spectra, wall shear stresses, and turbulent dissipation rates. *Front. Physiol.* **11**, 577188.

Bujard, T., Giorgio-Serchi, F. & Weymouth, G.D. 2021 A resonant squid-inspired robot unlocks biological propulsive efficiency. *Sci. Robot.* **6**, eabd2971.

CHOI, D. & PARK, H. 2018 Flow around in-line sphere array at moderate Reynolds number. *Phys. Fluids* **30**, 097104.

CHOI, D. & PARK, H. 2022 Flow–structure interaction of a starting jet through a flexible circular nozzle. *J. Fluid Mech.* **949**, A39.

CHOI, K. & PARK, H. 2021 Interfacial phenomena of the interaction between a liquid–liquid interface and rising bubble. *Exp. Fluids* **62**, 126.

CHRISTIANSON, C., CUI, Y., ISHIDA, M., BI, X., ZHU, Q., PAWLAK, G. & TOLLEY, M.T. 2020 Cephalopod-inspired robot capable of cyclic jet propulsion through shape change. *Bioinspir. Biomim.* **16**, 016014.

DABIRI, J.O. & GHARIB, M. 2005 Starting flow through nozzles with temporally variable exit diameter. *J. Fluid Mech.* **538**, 111–136.

DAS, P., GOVARDHAN, R.N. & ARAKERI, J.H. 2018 Unsteady two-dimensional jet with flexible flaps at the channel exit. *J. Fluid Mech.* **845**, 462–498.

GAO, L., WANG, X., SIMON, C.M. & CHYU, M.K. 2020 Development of the impulse and thrust for laminar starting jets with finite discharged volume. *J. Fluid Mech.* **902**, A27.

GERULLIS, P. & SCHUSTER, S. 2014 Archerfish actively control the hydrodynamics of their jets. *Curr. Biol.* **24**, 2156–2160.

GHARIB, M., RAMBOD, E. & SHARIFF, K. 1998 A universal time scale for vortex ring formation. *J. Fluid Mech.* **360**, 121–140.

KRAUS, H. 1967 *Thin Elastic Shells: An Introduction to the Theoretical Foundations and the Analysis of their Static and Dynamic Behavior*. Wiley.

KRIEG, M. & MOHSENI, K. 2013 Modelling circulation, impulse and kinetic energy of starting jets with non-zero radial velocity. *J. Fluid Mech.* **719**, 488–526.

KRUEGER, P.S. & GHARIB, M. 2003 The significance of vortex ring formation to the impulse and thrust of a starting jet. *Phys. Fluids* **15**, 1271–1281.

LIMBOURG, R. & NEDIĆ, J. 2021 Formation of an orifice-generated vortex ring. *J. Fluid Mech.* **913**, A29.

LINDEN, P.F. 2011 The efficiency of pulsed-jet propulsion. *J. Fluid Mech.* **668**, 1–4.

MAENG, H. & PARK, H. 2021 An experimental study on the heat transfer by a single bubble wake rising near a vertical heated wall. *Intl J. Heat Mass Transfer* **165**, 120590.

MOSLEMI, A.A. & KRUEGER, P.S. 2011 The effect of Reynolds number on the propulsive efficiency of a biomorphic pulsed-jet underwater vehicle. *Bioinspir. Biomim.* **6**, 026001.

O'DOR, R., PÖRTNER, H.O. & SHADWICK, R.E. 1990 Squid as elite athletes: locomotory, respiratory, and circulatory integration. In *Squid as Experimental Animals* (ed. D.L. Gilbert, W.J. Adelman & J.M. Arnold), pp. 481–503. Springer.

OLCAY, A.B. & KRUEGER, P.S. 2008 Measurement of ambient fluid entrainment during laminar vortex ring formation. *Exp. Fluids* **44**, 235–247.

RUIZ, L.A., WHITTLESEY, R.W. & DABIRI, J.O. 2011 Vortex-enhanced propulsion. *J. Fluid Mech.* **668**, 5–32.

SAFFMAN, P.G. 1955 *Vortex Dynamics*. Cambridge University Press.

SCHOFIELD, Z., BAKSAMAWI, H.A., CAMPOS, J., ALEXIADIS, A., NASH, G.B., BRILL, A. & VIGOLO, D. 2020 The role of valve stiffness in the insurgence of deep vein thrombosis. *Commun. Mater.* **1**, 65.

SCHOTT, F., BAUMBACH, G., STRAUB, D., THORWARTH, H. & VOGT, U. 2022 Novel metal mesh filter equipped with pulse-jet regeneration for small-scale biomass boilers. *Biomass Bioenergy* **163**, 106520.

SHIM, J., JOE, Y.H. & PARK, H.S. 2017 Influence of air injection nozzles on filter cleaning performance of pulse-jet bag filter. *Powder Technol.* **322**, 250–257.

STAAF, D.J., GILLY, W.F. & DENNY, M.W. 2014 Aperture effects in squid jet propulsion. *J. Expl Biol.* **217**, 1588–1600.